

# Impact of chaotic magnetic field on physical properties of rotating neutron stars

M. Lawrence Patterson<sup>a,1</sup>, Freddy P. Zen<sup>b,1,2</sup>, Hadyan L. Prihadi<sup>c,3,2</sup>,  
Muhammad F. A. R. Sakti<sup>d,4</sup>, Getbogi Hikmawane<sup>e,1,2</sup>

<sup>1</sup>Theoretical High Energy Physics Group, Department of Physics, Institut Teknologi Bandung, Jl. Ganesha 10, Bandung 40132, Indonesia

<sup>2</sup>Indonesia Center for Theoretical and Mathematical Physics (ICTMP), Institut Teknologi Bandung, Jl. Ganesha 10, Bandung 40132, Indonesia

<sup>3</sup>Research Center for Quantum Physics, National Research and Innovation Agency (BRIN), South Tangerang 15314, Indonesia

<sup>4</sup>High Energy Physics Theory Group, Department of Physics, Faculty of Science, Chulalongkorn University, Bangkok 10330, Thailand

**Abstract** Observations reveal that magnetic fields on neutron stars (NSs) are in the range of  $10^{8-15}$  G. Apart from being celestial bodies, NSs are normally rotating. In this work, we study the impact of a chaotic magnetic field on the physical properties of the rotating NSs. i.e. mass, radius, Kepler frequency, and moment of inertia. We employ an equation of state (EOS) of NSs with the relativistic mean-field (RMF) model. Hartle-Thorne formalism as an approximation of the rotating NSs is utilized. We find that the magnetic field can decrease radius of NS. NSs formed with magnetic field exhibit a lower maximum mass compared to those without magnetic field. In contrast, the increment of the magnetic field can increase the compactness and deformation of rotating NSs. The presence of chaotic magnetic field enhances the Kepler frequency of rotating NSs, whereas it simultaneously tend to decreases their moment of inertia. The moment of inertia of rotating NSs is consistent with the constraint range obtained from pulsar mass measurements, gravitational wave event data, and X-ray observations of emissions from hotspots on NS surfaces measured by NICER.

## 1 Introduction

It has been widely understood that the evolution of the massive stars whose mass is  $8-25 M_{\odot}$  ends when neutron stars (NSs) form. The corresponding formation is due to the stars' gravitational collapse during Type-

<sup>a</sup>e-mail: m.pattersons@proton.me

<sup>b</sup>e-mail: fpzen@fi.itb.ac.id

<sup>c</sup>e-mail: hady001@brin.go.id

<sup>d</sup>e-mail: fitrahalfian@gmail.com

<sup>e</sup>e-mail: getbogi@fi.itb.ac.id

II, Ib, or Ic supernova explosion phenomena [1, 2]. NSs are compact remnants of evolved stars, with degenerate fermions compressed by strong gravitational fields [3]. The stabilizing effect of gravity allows long-time-scale weak interactions (such as electron captures) to reach equilibrium, forming matter that is neutron-rich [4]. These stars cover an extensive density range, roughly several times of nuclear density ( $n_0 \sim 10^{14}$  gm/cc), throughout their outer crust to their inner core [5]. NSs are normally rotating as all celestial objects tend to naturally always rotate due to the law of angular momentum conservation [6]. When rotating NSs are highly magnetized, they are recognized as pulsars [7, 8, 9, 10].

NSs have a wide range of magnetic fields. Observations indicate that magnetic fields on NSs are at least in the range of  $10^{8-15}$  G [3]. It is important to note that the direct observation of the magnetic field in NSs' cores remains unachieved. However, theoretical predictions suggest that the strengths of the magnetic fields in NSs' cores are in the order of  $10^{18}$  G to  $10^{20}$  G [11, 12, 13]. New classes of pulsars such as Anomalous X-ray pulsars (AXPs) and Soft-Gamma Repeater pulsars (SGRs) have been identified producing vast magnetic fields. SGR is associated with remnants of a supernova, which is a young NS [14]. Highly magnetized NSs, i.e. magnetars, are typically slowly rotating NSs whose emission is thought to be powered by the decay of their large ( $\geq 10^{12}$  G) magnetic fields, much greater than pulsars [15]. As well as their extreme magnetic fields, magnetars are thought to have core temperature to be well above  $10^9$  K [16]. Moreover, observations on some AXPs also indicate that magnetic field of AXPs surface is around  $10^{14} - 10^{15}$  G [14].

Konno et al. [17] calculated the deformation of NSs resulting from rotation and the presence of magnetic

fields. In their analysis, a polytropic equation of state (EOS) was employed. Their findings indicate that for magnetars, the deformation induced by magnetic fields is dominant, whereas for typical pulsars, the magnetic effect is negligible. Mallick & Schramm [18] investigated mass corrections and the deformation of NSs under the influence of magnetic fields, treating the magnetic field as an anisotropy in the energy-momentum tensor (EMT). Interestingly, despite focusing on static NSs, their approach was based on the Hartle-Thorne (HT) formalism [19, 20], which is typically applied to rotating relativistic stars. In their work, magnetic perturbations in static configurations were treated analogously to rotational perturbations, following the HT approximation. They considered both very stiff and very soft EOS models in their study. Lopes & Menezes [21] explored the effects of chaotic magnetic fields on NSs. A key advantage of incorporating a chaotic magnetic field lies in the elimination of anisotropy, simplifying the mathematical formulation. They also introduced an ansatz where the magnetic field is coupled to the energy density of the NS. For their EOS models, they utilized two variations: one including hyperons and one without hyperons. However, the rotation of NSs was not considered in their analysis.

On the other hand, in Newtonian theory, there exists a maximum rotational frequency for stars composed of perfect fluid, where gravitational and centrifugal forces are in equilibrium at their equators. This maximum frequency is proportional to the square root of the ratio of their masses to their radii [22]. In the context of general relativity (GR), the angular velocity of NSs is limited by the Kepler frequency, a threshold determined by their mass and radius in static configurations [23, 24]. Notably, Refs. [22, 23, 24] provide specific calculations of the Kepler frequency.

Another significant property of NSs is their moment of inertia, which offers insights into their internal structure and EOS. Given the link between the EOS and moment of inertia, approximate methods for estimating it in static models, particularly for stiff EOS scenarios, are feasible [25]. Furthermore, measuring the moment of inertia is crucial due to its universal correlation with compactness [26]. Rahmansyah et al. [26] calculated the moment of inertia of anisotropic NS which satisfies the constraints proposed by Landry et al. [27]. However, the magnetic field is not taken into account in their calculation of the moment of inertia.

Building on previous studies, we investigate the influence of the chaotic magnetic field on some physical properties of rotating NSs, i.e. mass, radius, Kepler frequency, and moment of inertia. In particular, for the moment of inertia, we adopt the very slow rotation ap-

proximation with angular velocity  $\Omega = 50 \text{ s}^{-1}$ . Under this condition, stellar deformation is neglected, as the stars remain nearly perfectly spherical, with eccentricity values approaching zero. This justifies the use of the standard moment of inertia formula for a spherical body. Such an approach has also been adopted in Refs. [26, 28]. The rotational aspects are modeled using the HT formalism, while the magnetic field is described by the Lopes-Menezes ansatz.

In general, NS has three parts with different compositions and density ranges i.e., outer crust, inner crust and the core [29]. These compositions are described by an EOS. Here we employ the relativistic mean-field (RMF) EOS with BSP parameter sets [30]. The algorithm of the numerical simulation follows the one used in Refs. [23, 31].

The remainder of this paper is organized as follows. In Section 2, we outline the formulations employed in this study. Section 3 presents the numerical results and a discussion of their implications. Finally, we provide a summary of our findings in Section 4.

## 2 Mathematical Formulations

To make the discussion self-contained, in Sect. 2.1, we briefly present the nuclear model used in this work; then in Sec 2.2, we shortly review the chaotic magnetic field of NSs; while the HT formalism is given in Sect. 2.2. It is important to note that in the mathematical formulations we use  $G = c = 1$ .

### 2.1 Nuclear Model

The Lagrangian density for the RMF model reads [30]

$$\mathcal{L} = \mathcal{L}_{NM} + \mathcal{L}_\sigma + \mathcal{L}_\omega + \mathcal{L}_\rho + \mathcal{L}_{\sigma\omega\rho}, \quad (1)$$

where  $\mathcal{L}_{NM}$  is the Lagrangian that describes the interactions of the nucleons through the mesons. It is given by

$$\begin{aligned} \mathcal{L}_{NM} = & \sum_{J=n,p} \bar{\Psi}_J [i\gamma^\mu \partial_\mu - (M - g_\sigma \sigma) \\ & - \left( g_\omega \gamma^\mu \omega_\mu + \frac{1}{2} g_\rho \gamma^\mu \tau \cdot \rho_\mu \right)] \Psi_J. \end{aligned} \quad (2)$$

Note that the sum is taken over the neutrons and protons. Here  $\tau$  are the isospin matrices. Moreover, the Lagrangian that describes the self-interactions for  $\sigma$ ,  $\omega$ , and  $\rho$  mesons can be written as,

$$\begin{aligned} \mathcal{L}_\sigma = & \frac{1}{2} (\partial_\mu \sigma \partial^\mu \sigma - m_\sigma^2 \sigma^2) - \frac{\kappa_3}{6M} g_\sigma m_\sigma^2 \sigma^3 \\ & - \frac{\kappa_4}{24M^2} g_\sigma^2 m_\sigma^2 \sigma^4, \end{aligned} \quad (3)$$

$$\mathcal{L}_\omega = -\frac{1}{4}\omega_{\mu\nu}\omega^{\mu\nu} + \frac{1}{2}m_\omega^2\omega_\mu\omega^\mu + \frac{1}{24}\zeta_0g_\omega^2(\omega_\mu\omega^\mu)^2, \quad (4)$$

$$\mathcal{L}_\rho = -\frac{1}{4}\rho_{\mu\nu}\cdot\rho^{\mu\nu} + \frac{1}{2}m_\rho^2\rho_\mu\cdot\rho^\mu, \quad (5)$$

Here,  $\omega_{\mu\nu}$  and  $\rho^{\mu\nu}$  are the field tensors corresponding to the  $\omega$  and  $\rho$  mesons, respectively. They are defined as  $\omega_{\mu\nu} = \partial_\mu\omega_\nu - \partial_\nu\omega_\mu$  and  $\rho^{\mu\nu} = \partial^\mu\rho^\nu - \partial^\nu\rho^\mu$ . Furthermore, the cross interactions of  $\sigma$ ,  $\omega$ , and  $\rho$  mesons are given by  $\mathcal{L}_{\sigma\omega\rho}$ , i.e.

$$\begin{aligned} \mathcal{L}_{\sigma\omega\rho} = & \frac{\eta_1}{2M}g_\sigma m_\omega^2\sigma\omega_\mu\omega^\mu + \frac{\eta_2}{4M^2}g_\sigma^2m_\omega^2\sigma^2\omega_\mu\omega^\mu \\ & + \frac{\eta_\rho}{2M}g_\sigma m_\rho^2\sigma\rho_\mu\cdot\rho^\mu \\ & + \frac{\eta_{1\rho}}{4M^2}g_\sigma^2m_\rho^2\sigma^2\rho_\mu\cdot\rho^\mu \\ & + \frac{\eta_{2\rho}}{4M^2}g_\omega^2m_\rho^2\omega_\mu\omega^\mu\rho_\mu\cdot\rho^\mu. \end{aligned} \quad (6)$$

**Table 1** BSP parameter sets [30] for the RMF model.

	Value
$g_\sigma/4\pi$	0.8764
$g_\omega/4\pi$	1.1481
$g_\rho/4\pi$	1.0508
$\kappa_3$	1.0681
$\kappa_4$	14.9857
$\eta_1$	0.0872
$\eta_2$	3.1265
$\eta_\rho$	0.0
$\eta_{1\rho}$	0.0
$\eta_{2\rho}$	53.7642
$\zeta_0$	0.0
$m_\sigma/M$	0.5383
$m_\omega/M$	0.8333
$m_\rho/M$	0.8200

The values of the free parameters of the Lagrangian for this model are listed in Table 1, while the predicted properties at saturation density—namely the binding energy per baryon ( $B/A$ ), incompressibility ( $K$ ), symmetry energy ( $S_0$ ), the slope of the symmetry energy ( $L$ ), and saturation density ( $n_0$ ) itself—are summarized in Table 2. The constraints for the predicted values at saturation density are taken from Refs. [24, 26, 32].

For the crust of NSs, the one in Refs [33, 34] is used. At the core-crust transition, the pressures of the core and the inner crust are matched. The core-crust transition occurs at the transition nuclear density  $n_t = 0.087 \text{ fm}^{-3}$  and transition pressure  $p_t = 0.29 \text{ MeV fm}^{-3}$  [26].

It is important to note that the effect of the magnetic field on the EOS is not taken into account, as our focus is solely on investigating the impact of the chaotic magnetic field on general relativistic aspects of NSs and their implication on the NSs' physical properties.

**Table 2** Predictions for the RMF EOS with BSP parameter sets at saturation density. the constraints are taken from Refs. [24, 26, 32].

Physical Quantities	Constraints	This Model
$n_0 \text{ (fm}^{-3}\text{)}$	0.148–0.170	0.149
$K \text{ (MeV)}$	220–260	230.97
$S_0 \text{ (MeV)}$	28.5–34.9	28.86
$B/A \text{ (MeV)}$	15.8–16.5	15.90
$L \text{ (MeV)}$	44–116	50.00

## 2.2 Chaotic Magnetic Field of Neutron Stars

Generally, chaotically tangled magnetic field lines are thought to be present throughout astrophysical plasmas: planets, stars, accretion discs, galaxies, clusters of galaxies, and the intergalactic medium [35]. In nature, chaotic magnetic fields could be generated by asymmetric current configuration [36].

It has been widely understood that the magnetic field could generate anisotropy within NSs [11, 14, 18]. This problem would make the HT formalism for rotational configuration becomes more complex (please see Refs. [1, 37, 38]). For the magnetic field  $B$  in the  $z$ -direction, it is well-known that the stress tensor is written in the form:  $\text{diag}(\frac{B^2}{8\pi}; \frac{B^2}{8\pi}; -\frac{B^2}{8\pi})$ , being non identical [21]. In Ref. [39], it is argued that the effect of a magnetic field can be described using the concept of pressure only in the case of a small-scale chaotic field. Under this condition, the pressure due to the magnetic field  $p_B$  is shown to be consistent with field theory. Ref. [21] agreed to this argument. Now  $p_B$  reads

$$p_B = \frac{1}{3} < T_j^j > = \frac{1}{3} \left( \frac{B^2}{8\pi} + \frac{B^2}{8\pi} - \frac{B^2}{8\pi} \right) = \frac{B^2}{24\pi}, \quad (7)$$

where  $T_j^j$  denotes the spatial components of the EMT. With this formulation in our hand, we can avoid the anisotropy which is caused by the appearance of magnetic field. The total energy density  $\epsilon$  and total pressure  $p$  now write

$$\epsilon = \epsilon_m + \frac{B^2}{8\pi}, \quad (8)$$

$$p = p_m + \frac{B^2}{24\pi}, \quad (9)$$

where the subscript  $m$  stands for the matter contribution.

An ansatz of the magnetic field is proposed in Ref. [21], i.e.

$$B = B_0 \left( \frac{\epsilon_m}{\epsilon_0} \right)^\gamma + B_{\text{surf}}. \quad (10)$$

Here  $B_0$  can be interpreted as the magnetic field at the center of the star,  $\epsilon_0$  is the energy density at the center

of the NS with maximum mass when the magnetic field is zero,  $\gamma$  is any positive number (in this work we use  $\gamma = 3, 5$ , and  $6$ ), and  $B_{surf}$  is the magnetic field at the surface of the NSs.

### 2.3 Hartle-Thorne Formalism for Rotating Relativistic Stars

The details of the HT formalism can be found in the original papers [19, 20]. Other interesting additional discussions on the formalism can be referred to Refs. [1, 31, 37, 38]. Here we present only a little discussion and the necessary equations to calculate some physical properties, i.e. mass, radius, Kepler frequency, and moment of inertia. This is especially useful to help the readers who are not familiar with the HT formalism.

It has to be noted that based on Eq. (8) and Eq. (9), it can be seen that the total energy density and total pressure arising from the matter and the presence of a magnetic field can be redefined by introducing  $\epsilon$  and  $p$ . Therefore, in this subsection, the definitions of  $\epsilon$  and  $p$  also encompass the total contributions from both matter and the magnetic field. Consequently, the formulation of HT presented in this subsection is indirectly modified by the presence of the magnetic field. Although this modification is not explicitly apparent, the contribution of the magnetic field is embedded within  $\epsilon$  and  $p$ .

In HT formalism, the metric reads [1, 19, 20, 31]

$$ds^2 = -e^{2\nu} dt^2 + e^{2\lambda} dr^2 + e^{2\psi} (d\phi - \omega dt)^2 + e^{2\mu} d\theta^2, \quad (11)$$

where  $\omega$  is the angular velocity of the local inertial frame, which is proportional to the star's angular velocity  $\Omega$  relative to a distant observer. In this case,  $\omega$  and  $\Omega$  satisfy  $\omega = \Omega - \bar{\omega}$ , where  $\bar{\omega}$  is the angular velocity of the star relative to the local inertial frame.

Due to rotational perturbation, the exponential functions in Eq. (11) are expanded as the following:

$$e^{2\nu} = e^{2\varphi} [1 + 2(h_0 + h_2 P_2(\cos \theta))], \quad (12)$$

$$e^{2\lambda} = \left[ 1 + \frac{2}{r} (m_0 + m_2 P_2(\cos \theta)) \left( 1 - \frac{2m(r)}{r} \right)^{-1} \right] \times \left( 1 - \frac{2m(r)}{r} \right)^{-1} \quad (13)$$

$$e^{2\psi} = r^2 \sin^2 \theta [1 + 2(v_2 - h_2) P_2(\cos \theta)], \quad (14)$$

$$e^{2\mu} = r^2 [1 + 2(v_2 - h_2) P_2(\cos \theta)]. \quad (15)$$

Here  $h_0$ ,  $h_2$ ,  $m_0$ ,  $m_2$ , and  $v_2$  are functions of perturbation due to rotation;  $P_2(\cos \theta)$  is the second order of

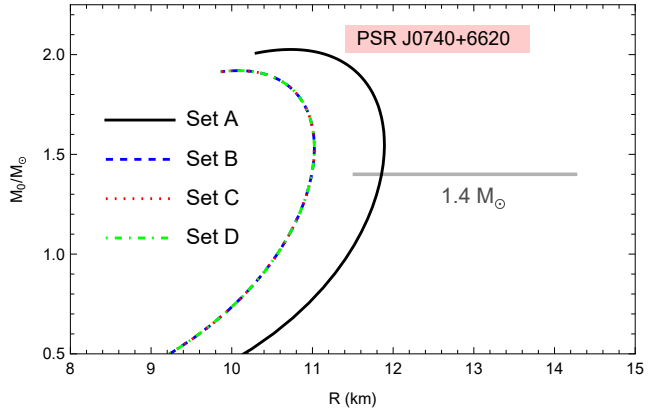


**Fig. 1** Mass-radius relation of NSs for static configuration with different parameter sets of chaotic magnetic field strengths.

Legendre polynomial;  $e^{2\varphi}$  is a function which is constrained by

$$\frac{d\varphi}{dr} = \frac{m + 4\pi r^3 p}{r(r - 2m)}, \quad (16)$$

where  $m$  is the mass function which is constrained by

$$\frac{dm}{dr} = 4\pi r^2 \epsilon. \quad (17)$$

The equilibrium equation of the relativistic bodies is given by the Tolman-Oppenheimer-Volkoff (TOV) equation [1, 19, 40], i.e.

$$\frac{dp}{dr} = -(\epsilon + p) \frac{d\varphi}{dr}. \quad (18)$$

For a rotating configuration,  $\bar{\omega}$  can be calculated by solving the following equation [19]:

$$\frac{1}{r^4} \frac{d}{dr} \left( r^4 j \frac{d\bar{\omega}}{dr} \right) + \frac{4}{r} \frac{dj}{dr} = 0, \quad (19)$$

where

$$j = e^{-\varphi} \left( 1 - \frac{2m}{r} \right)^{1/2}. \quad (20)$$

The boundary condition at  $r = 0$  is  $\bar{\omega} = \omega_c$ , where  $\omega_c$  can be chosen arbitrarily.

It is important to note that Eqs. (16)–(18) deal with static configuration. Moreover, due to the rotation, the radius of the star is deformed. To obtain the mass and radius corrections of the rotating NS, we have to employ Einstein field equation

$$R_\nu^\mu - \frac{1}{2} \mathcal{R} \delta_\nu^\mu = 8\pi T_\nu^\mu, \quad (21)$$

where  $R_\nu^\mu$  is Ricci tensor,  $\mathcal{R}$  is Ricci scalar,  $\delta_\nu^\mu$  is Kronecker delta, and  $T_\nu^\mu$  denotes the EMT.

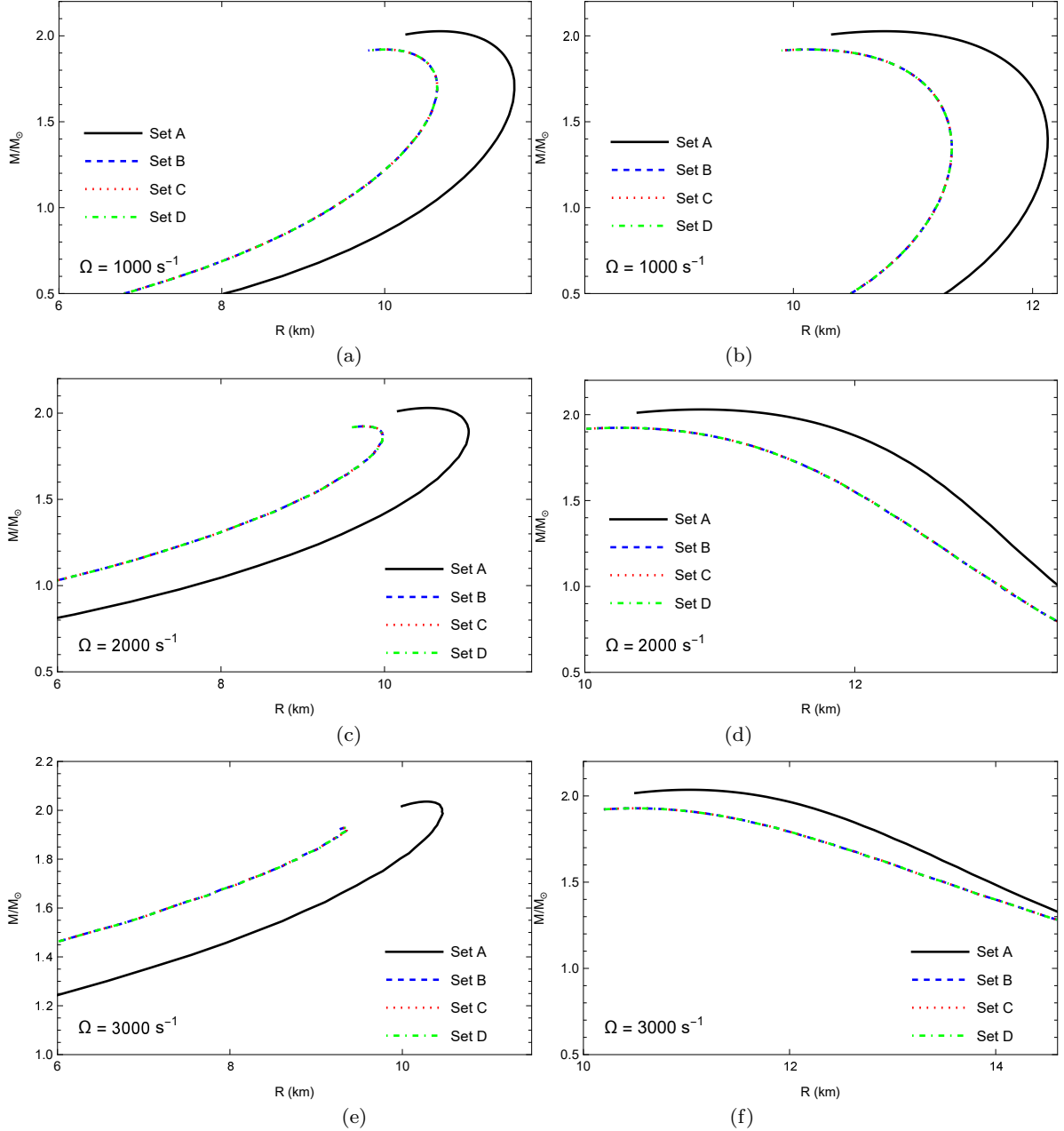


**Fig. 2** Mass-radius relation of NSs for (a) polar radius at  $\Omega = 1000 \text{ s}^{-1}$ , (b) equatorial radius at  $\Omega = 1000 \text{ s}^{-1}$ , (c) polar radius at  $\Omega = 2000 \text{ s}^{-1}$ , (d) equatorial radius at  $\Omega = 2000 \text{ s}^{-1}$ , (e) polar radius at  $\Omega = 3000 \text{ s}^{-1}$ , and (f) equatorial radius at  $\Omega = 3000 \text{ s}^{-1}$ .

By calculating the Einstein field equation, for the  $(tt)$  component of the  $l = 0$  order, we can obtain

$$\frac{dm_0}{dr} = 4\pi r^2 \frac{d\epsilon}{dp} (\epsilon + p) \mathcal{P}_0 + \frac{1}{12} j^2 r^4 \left( \frac{d\bar{\omega}}{dr} \right)^2 - \frac{1}{3} r^3 \left( \frac{dj^2}{dr} \right) \bar{\omega}^2. \quad (22)$$

From the  $(rr)$  component of the  $l = 0$  order, we can obtain

$$\begin{aligned} \frac{d\mathcal{P}_0}{dr} = & -\frac{m_0 (1 + 8\pi r^2 p)}{(r - 2m)^2} - \frac{8\pi r^2 (\epsilon + p)}{2(r - 2m)} \mathcal{P}_0 + \frac{1}{12} \\ & \times \frac{r^4 j^2}{r - 2m} \left( \frac{d\bar{\omega}}{dr} \right)^2 + \frac{1}{3} \left[ \frac{d}{dr} \left( \frac{r^3 j^2 \bar{\omega}^2}{r - 2m} \right) \right]. \end{aligned} \quad (23)$$

Here  $\mathcal{P}_0$  is originally the 0th-order of expansion of pressure perturbation factor  $\mathcal{P} = \mathcal{P}_0 + \mathcal{P}_2 P_2(\cos\theta)$ . The boundary conditions at  $r = 0$  are  $m_0(0) = 0$  and  $\mathcal{P}_0(0) = 0$ .

Mass correction  $\delta M$  of the star is given by

$$\delta M = m_0(R) + \frac{L^2}{R^3}, \quad (24)$$

where  $R$  denotes the radius of the star, and  $L$  denotes the angular momentum. In Ref. [20], there is a relation

$$\Omega = \bar{\omega}(R) + \frac{2L}{R^3}, \quad (25)$$

so we can obtain

$$L = \frac{R^3}{2}(\Omega - \bar{\omega}(R)). \quad (26)$$

Alternatively, angular momentum can be calculated as [41]

$$L = \frac{8\pi}{3} \int_0^R dr r^4 \frac{\epsilon(r) + p(r)}{\sqrt{1 - 2m(r)/r}} \bar{\omega}(r) e^{-\varphi(r)}. \quad (27)$$

Thus, the total mass reads

$$M = M_0 + \delta M, \quad (28)$$

where  $M_0$  is the mass of NSs within static configuration which is obtained by solving Eqs. (16)–(18) simultaneously.

From the  $(\theta\theta)$ ,  $(\phi\phi)$ ,  $(\theta r)$ , and  $(rr)$  components of the  $l = 2$  order of Einstein field equation, we obtain

$$\begin{aligned} \frac{dv_2}{dr} &= -2 \frac{d\varphi}{dr} h_2 + \left( \frac{1}{r} + \frac{d\varphi}{dr} \right) \\ &\times \left[ -\frac{1}{3} r^3 \frac{dj^2}{dr} \bar{\omega}^2 + \frac{1}{6} j^2 r^4 \left( \frac{d\bar{\omega}}{dr} \right)^2 \right], \end{aligned} \quad (29)$$

$$\begin{aligned} \frac{dh_2}{dr} &= -2 \frac{d\varphi}{dr} h_2 + \frac{[8\pi r(\epsilon + p) - \frac{4m}{r^2}]}{(r - 2m) \left( 2 \frac{d\varphi}{dr} \right)} h_2 \\ &- \frac{4v_2}{r(r - 2m)} \left( 2 \frac{d\varphi}{dr} \right)^{-1} + \frac{r^3 j^2}{6} \\ &\times \left[ \frac{d\varphi}{dr} r - \frac{1}{(r - 2m) \left( 2 \frac{d\varphi}{dr} \right)} \right] \left( \frac{d\bar{\omega}}{dr} \right)^2 \\ &- \frac{r^2 \bar{\omega}^2}{3} \left[ \frac{d\varphi}{dr} + \frac{1}{(r - 2m) \left( 2 \frac{d\varphi}{dr} \right)} \right] \frac{dj^2}{dr}. \end{aligned} \quad (30)$$

The boundary conditions at  $r = 0$  are  $v_2(0) = 0$  and  $h_2 = 0$ .

There exists a formula [1, 19]

$$\mathcal{P}_2 = -h_2 - \frac{1}{3} r^2 e^{-2\varphi} \bar{\omega}^2. \quad (31)$$

The radius correction of the star is given by

$$\delta r = \xi_0(R) + \xi_2(R) P_2(\cos \theta), \quad (32)$$

**Table 3** Parameter sets of the magnetic fields

	$\gamma$
Set A	$B = 0$
Set B	3
Set C	5
Set D	6

where

$$\begin{aligned} \xi_0 &= -\mathcal{P}_0(\epsilon + p) \left( \frac{dp}{dr} \right)^{-1}, \\ \xi_2 &= -\mathcal{P}_2(\epsilon + p) \left( \frac{dp}{dr} \right)^{-1}. \end{aligned} \quad (33)$$

Finally, we can calculate the radius of the pole  $R_{POL}$  and the radius of the equator  $R_{EQ}$  [1, 24]

$$R_{POL} = R + \xi_0 + \xi_2, \quad (34)$$

$$R_{EQ} = R + \xi_0 - \frac{\xi_2}{2}. \quad (35)$$

This allows us to calculate the eccentricity

$$e = \sqrt{1 - \frac{R_{POL}^2}{R_{EQ}^2}}. \quad (36)$$

Furthermore, in the original papers of HT formalism [19, 20], the maximum angular velocity of a rotating body within Newtonian gravity is mentioned, i.e.

$$\Omega_{max} = \sqrt{M_0/R^3}. \quad (37)$$

However, in the context of GR, the maximum angular velocity of NSs (which is called as Kepler frequency) is approximated by [24]

$$\Omega_K = 0.65 \sqrt{M_0/R^3}. \quad (38)$$

Moreover, another important physical quantity to consider is the moment of inertia. With the angular momentum  $L$  and the angular velocity relative to the distant observers  $\Omega$  in our hands, we can determine the moment of inertia

$$I = \frac{L}{\Omega}. \quad (39)$$

### 3 Results and Discussion

We numerically solved all differential equations using Euler method. For the value of  $\Omega$ , we consider  $\Omega = 1000$   $\text{s}^{-1}$ ,  $\Omega = 2000$   $\text{s}^{-1}$ , and  $\Omega = 3000$   $\text{s}^{-1}$ . However, except for the calculation of the moment of inertia, we use  $\Omega = 50$   $\text{s}^{-1}$ , as we only employ the very slow rotation approximation for this purpose. For the initial value of  $\bar{\omega}$  (i.e.,  $\omega_c$ ), we adopt  $\omega_c = 80$   $\text{s}^{-1}$  in all cases

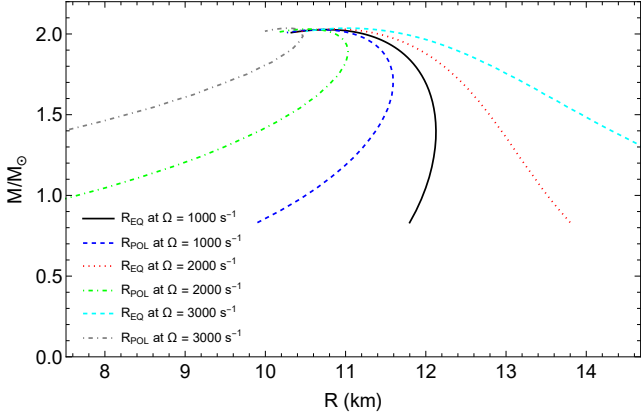


**Fig. 3** Mass-radius relation of the deformed NSs without magnetic field.

throughout this work, except in the calculation of the moment of inertia, where we set  $\omega_c$ . It is worth noting that the value  $\omega_c = 0$  used in our calculations is significantly smaller than the value used in Ref. [42], where  $\bar{\omega} = 3000 \text{ s}^{-1}$ . Moreover, it is also worth noting that  $\bar{\omega}(r)$  increases with  $r$ , which would result in a large  $\bar{\omega}$  value at the surface if a large initial  $\omega_c$  is chosen. On the other side, we have insight that according to Ref. [43], the HT formalism is accurate to better than 1 per cent even for the fastest millisecond pulsars. However, putting  $\bar{\omega}_c = 3000 \text{ s}^{-1}$  in the calculation is still potential to be dangerous, for the HT formalism is basically an approximation for slowly rotating relativistic stars. So our value of  $\bar{\omega}_c$  is safer than the one in Ref. [42].

If we compare our initial value of  $\bar{\omega}$ —excluding the one used for the moment of inertia calculation—to those in Ref. [1] and Ref. [23], which adopted  $\bar{\omega}_c = 0$ , our choice of  $\bar{\omega}_c = 80 \text{ s}^{-1}$  appears to be more realistic for modeling general rotating NSs. In contrast, their assumption of  $\bar{\omega}_c = 0$  is more appropriate only for very slowly rotating neutron stars. A similar choice of  $\omega_c$  and the reasoning behind it have also been emphasized by the authors in Ref. [31]. We set the limitation of  $\Omega$  to be  $3000 \text{ s}^{-1}$  in our analysis.

Moreover, the parameter sets for the magnetic field employed in this study are summarized in Table 3. We consider both scenarios: without and with the presence of a magnetic field. For the cases where the magnetic field is present, we vary the parameter  $\gamma$  with values of 3, 5, and 6. It is also important to note that although  $\gamma$  is formally a free parameter and can, in principle, take any positive value, choosing a very small value (e.g., of the order of  $10^{-3}$ ) is problematic. In such cases, the magnetic field becomes strongly dominated by the constant component  $B_0$ , making it effectively resemble a uniform magnetic field, which is unphysical in the context of our model.

It has to be noted that the impact of varying the parameter  $\gamma$  is not significant. As shown in Table 4, we provide examples of how changes in  $\gamma$  affect several key quantities, namely the maximum mass  $M^{\max}$ , the average radius at maximum mass  $\bar{R}^{\max}$ , and the average radius at the canonical mass  $\bar{R}^{1.4}$ . We adopt the definition of average radius  $\bar{R}$  from Ref. [1], given by  $\bar{R} = \frac{R_{\text{POL}} + R_{\text{EQ}}}{2}$ . In this context, investigating the canonical mass is particularly relevant, as observational data suggest that NSs predominantly reside within a relatively narrow mass range around  $1.4M_{\odot}$  [44]. As shown in Table 4, the variation of  $\gamma$  affects the average radius at both the maximum mass and the canonical mass only at the order of  $10^{-5}$ , and even then, only for a subset of the cases. Most of the values remain unchanged. In fact, the maximum mass values are completely unaffected by variations in  $\gamma$ , indicating that its influence on the overall stellar structure is minimal within the explored range.

Fig. 1 presents the mass-radius relationship of NSs in a static configuration. This relation purely comes from TOV equation. From the relation, we can see that the presence of a chaotic magnetic field can reduce the radius of NSs, as indicated by the leftward shift of the curves with the appearance of magnetic field strength, suggesting that a chaotic magnetic field can contribute to greater compactness of the stars. Compactness, defined as the mass-to-radius ratio, is directly influenced by this field. Notably, the maximum mass of the NSs also decreases when the magnetic field appears.

Furthermore, when comparing our results with previous works that also employ chaotic magnetic fields using the same ansatz—such as Refs. [21, 45, 46]—a notable difference arises. While those studies report that the presence of chaotic magnetic fields allows for NSs with higher maximum masses, our results show a reduction in the maximum mass when magnetic fields are included. This discrepancy may be attributed to the fact that we do not include the magnetic field in the EOS, whereas the aforementioned studies do. As a result, their EOS becomes intrinsically stiffer in the presence of magnetic fields, which naturally leads to higher maximum masses.

Nevertheless, in terms of the shape of the mass-radius relation, particularly when varying  $\gamma$  within the range of 3 to 6, our results are still in qualitative agreement with the aforementioned studies. For example, while Ref. [45] shows more noticeable deviations between curves with different  $\gamma$  values, the results in Refs. [21] and [46] display behavior more similar to ours, where the differences are relatively minor and the curves seem to coincide. These variations may also stem from differences in the underlying EOS models, as it is well

**Table 4** Macroscopic properties of neutron stars under different magnetic field configurations. The quantities are the maximum mass  $M^{\max}$  (in  $M_{\odot}$ ), average radius at maximum mass  $\bar{R}^{\max}$  (in km), eccentricity at maximum mass  $e^{\max}$ , and central energy density at maximum mass  $\epsilon_c^{\max}$  (in MeV fm $^{-3}$ ). Additional columns show the corresponding values at  $1.4M_{\odot}$ .

	$M^{\max}/M_{\odot}$	$\bar{R}^{\max}$ (km)	$e^{\max}$	$\epsilon_c^{\max}$ (MeV fm $^{-3}$ )	$\bar{R}^{1.4}$ (km)	$e^{1.4}$	$\epsilon_c^{1.4}$ (MeV fm $^{-3}$ )
Set A at $\Omega = 0$	2.02575	10.74600	0	1309.60	11.85700	0	436.09
Set A at $\Omega = 1000$ s $^{-1}$	2.02686	10.73685	0.12437	1309.60	11.75275	0.34570	436.09
Set A at $\Omega = 2000$ s $^{-1}$	2.03020	10.70925	0.24618	1309.60	11.44003	0.63948	436.09
Set A at $\Omega = 3000$ s $^{-1}$	2.03576	10.66335	0.36303	1309.60	10.91882	0.84868	436.09
Set B at $\Omega = 0$	1.91962	10.09100	0	1487.32	10.98300	0	525.93
Set B at $\Omega = 1000$ s $^{-1}$	1.92058	10.07290	0.15953	1487.32	10.83280	0.40704	525.93
Set B at $\Omega = 2000$ s $^{-1}$	1.92345	10.01860	0.31385	1487.32	10.38220	0.73110	525.93
Set B at $\Omega = 3000$ s $^{-1}$	1.92824	9.92813	0.45821	1487.32	9.63110	0.92837	525.93
Set C at $\Omega = 0$	1.91962	10.09100	0	1487.32	10.98300	0	525.93
Set C at $\Omega = 1000$ s $^{-1}$	1.92058	10.07290	0.15953	1487.32	10.83280	0.40703	525.93
Set C at $\Omega = 2000$ s $^{-1}$	1.92345	10.01860	0.31384	1487.32	10.38220	0.73109	525.93
Set C at $\Omega = 3000$ s $^{-1}$	1.92824	9.92816	0.45820	1487.32	9.63120	0.92836	525.93
Set D at $\Omega = 0$	1.91962	10.09100	0	1487.33	10.98300	0	525.93
Set D at $\Omega = 1000$ s $^{-1}$	1.92058	10.07290	0.15953	1487.33	10.83280	0.40703	525.93
Set D at $\Omega = 2000$ s $^{-1}$	1.92345	10.01864	0.31384	1487.33	10.38218	0.73109	525.93
Set D at $\Omega = 3000$ s $^{-1}$	1.92824	9.92816	0.45820	1487.33	9.63115	0.92837	525.93

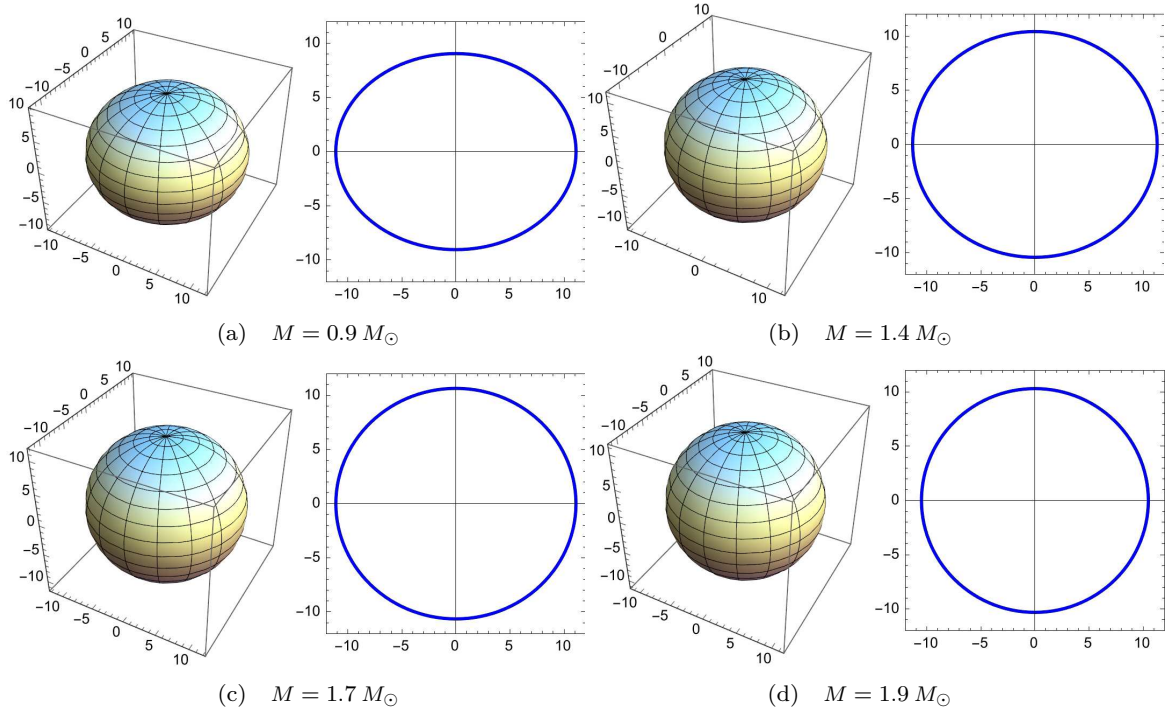


**Fig. 4** Illustrations of 3- and 2-dimensional deformation of neutron stars in each particular mass when  $\gamma = 3$  and  $\Omega = 1000$  s $^{-1}$ .

known that different EOS models can lead to significantly different outcomes in NS structure calculations [47].

In addition to the nuclear matter constraints, we also consider astrophysical constraints in this work, namely those related to PSR J0740+6620 and the radius at the canonical mass. PSR J0740+6620 has a mass of  $2.08 \pm 0.07 M_{\odot}$  [48], with a radius of  $12.39^{+0.98}_{-1.30}$  km [49].

As shown in Fig. 1, the maximum mass of NSs without magnetic fields satisfies the lower bound of the mass constraint, while the radius constraint is not fulfilled. NSs with magnetic fields fail to meet both constraints. Regarding the radius at canonical mass, neutron stars without magnetic fields satisfy the constraint, whereas those with magnetic fields do not. The exploration of

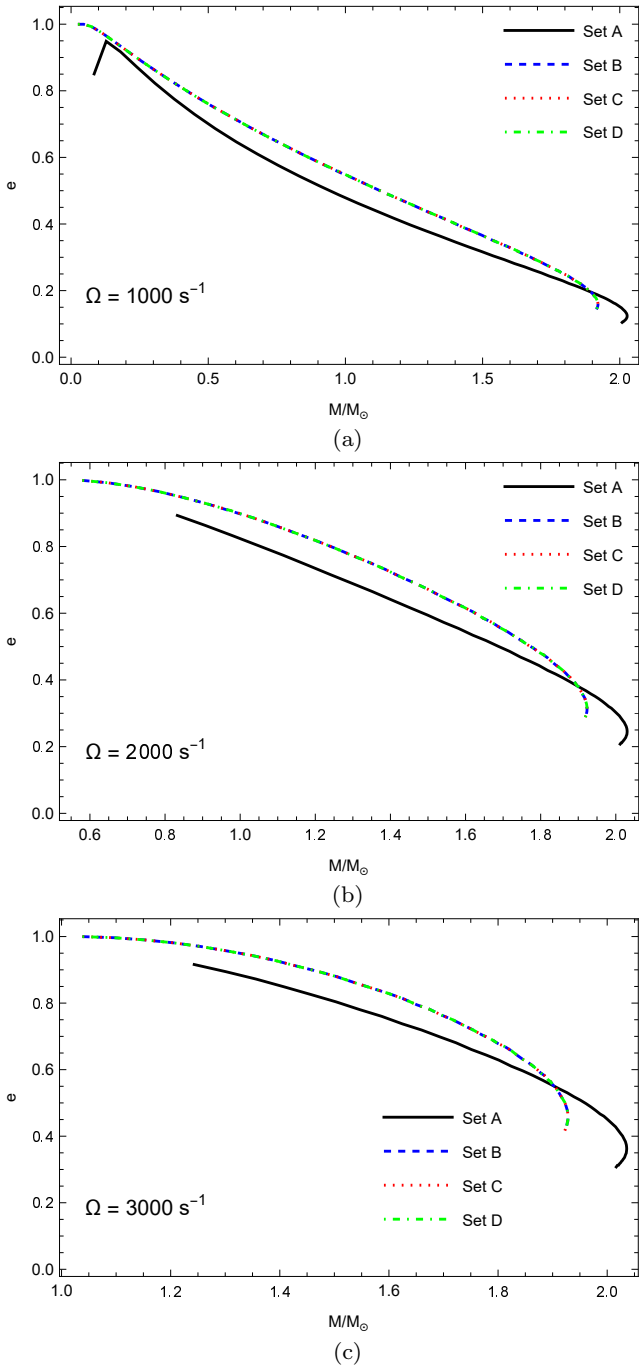


**Fig. 5** Eccentricity of NSs at (a)  $\Omega = 1000 \text{ s}^{-1}$ , (b)  $\Omega = 2000 \text{ s}^{-1}$ , and (c)  $\Omega = 3000 \text{ s}^{-1}$  as a function of mass.

an EOS that satisfies all nuclear and astrophysical constraints is left for future work.

Fig. 2 shows the polar and equatorial radii, indicating the deformation of rotating NSs. The deformation is less pronounced for the NSs with higher masses but becomes more evident for lower masses. This can be seen in the mass-radius relations of magnetized rotating NSs, where the curves in  $R_{POL}$  panels and  $R_{EQ}$  panels di-

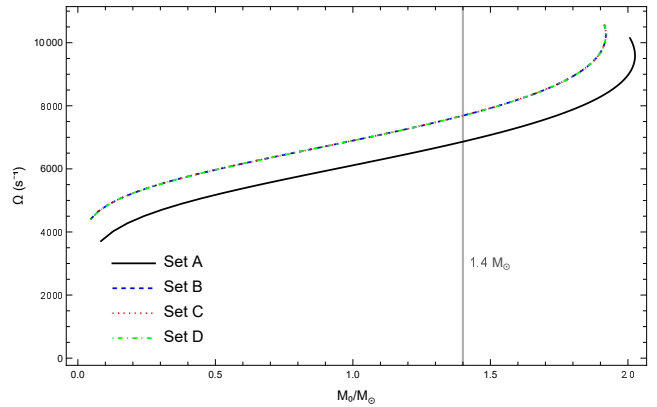


**Fig. 6** Kepler frequency of NSs as a function of mass.

verge significantly at lower mass values. A comparison with Fig. 3 which depicts rotating NSs without a magnetic field, reveals that deformation still occurs but with only slighter differences between the polar and equatorial radii. This deformation due to rotation is expected and is similar to the Earth's rotational deformation, where the polar radius is smaller than the equatorial radius [1]. The key takeaway from Fig. 2 and Fig. 3 is that the deformation induced by the magnetic field is much more significant than that caused by rotation. It is worth noting that even though the magnetic field strengthens the deformation of the stars, the magnetic field in the static case shown by Fig. 1 does not cause the deformation, because the deformation in this context comes from quadrupole order of HT formalism. Since the magnetic field is embedded within the energy density and pressure which exist in the perturbative terms of HT formalism, so the magnetic field could impact on the deformation of the rotating NSs.

It is important to emphasize that the rotational aspect also plays an important role to deform the NSs. As shown in Fig. 2 and Fig. 3, higher values of  $\Omega$  lead to a greater separation between the  $R_{POL}$  and  $R_{EQ}$  curves. Additionally, Fig. 2 demonstrates a substantial increase in deformation with the appearance of the magnetic field. This agrees with the findings in Ref. [11], where NSs were also deformed by the presence of a magnetic field, but the increase in deformation with the different configurations of magnetic field was less pronounced, leading to nearly coincident curves.

We present 3- and 2-dimensional illustrations of the NSs in Fig. 4. We take examples from the case of  $\gamma = 3$  with  $\Omega = 1000 \text{ s}^{-1}$ . At lower mass, the star's shape becomes very oblate. At  $M = 0.9 M_\odot$ ,  $R_{POL} = 9.04 \text{ km}$ , and  $R_{EQ} = 11.12 \text{ km}$ ; at  $M = 1.4 M_\odot$ ,  $R_{POL} = 10.34 \text{ km}$ , and  $R_{EQ} = 11.32 \text{ km}$ ; at  $M = 1.7 M_\odot$ ,  $R_{POL} = 10.64 \text{ km}$ , and  $R_{EQ} = 11.11 \text{ km}$ ; and at  $M = 1.9 M_\odot$ ,  $R_{POL} = 10.31 \text{ km}$ , and  $R_{EQ} = 10.50 \text{ km}$ . It

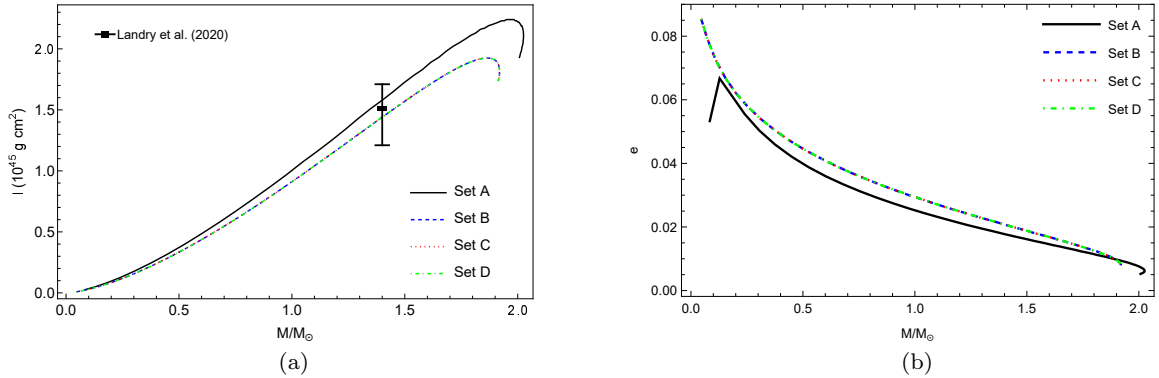


**Fig. 7** (a) Moment of inertia of NSs when  $\Omega = 50 \text{ s}^{-1}$ , (b) Eccentricity of the NSs when  $\Omega = 50 \text{ s}^{-1}$ . Here we use a constraint range for moment of inertia presented by Landry et al. [27].

is noteworthy to compare our results with those presented in Ref. [1]. The deformation of rotating NSs in our study is significantly more pronounced than in their findings, which are based on rotating NSs with anisotropic pressure of matter, but without considering the contribution of a magnetic field to the deformation. This fact strengthens our argument that the magnetic field strongly induces the deformation of rotating NSs.

The oblateness of NSs can also be characterized by their eccentricity  $e$ . In the context of a two-dimensional body, when the value of  $e$  approaches 0, the shape of the body tends to be circular. Conversely, as  $e$  approaches 1, the shape becomes more elliptical. Fig. 5 illustrates the relationship between mass and eccentricity. Both rotation and chaotic magnetic fields contribute to an increased deformation of NSs, as higher values of  $\Omega$  and the appearance of  $B$  drive the eccentricity  $e$  closer to 1.

Furthermore, it is noteworthy to analyze the trends of the eccentricity curves. At  $\Omega = 1000 \text{ s}^{-1}$ , the overall trend is consistent with the results reported in Ref. [24]. As the rotational frequency increases, the trends become more comparable to those presented in Ref. [1].

Fig. 6 illustrates the relationship between the  $M_0$  and the Kepler frequency of NSs. The Kepler frequency increases as the chaotic magnetic field appears, indicating that NSs with chaotic magnetic fields can rotate faster than those with weaker fields.

Previously, the mass and radius calculations revealed that rotating NSs with chaotic magnetic fields exhibit lower maximum masses and smaller radii. This finding suggests that, for NSs rotating at their respective Kepler frequencies, our results are consistent with the conservation of angular momentum. Specifically, the presence of magnetic fields is associated with a reduction in both maximum mass and radius, but an increase in the maximum angular velocity (i.e., the Kepler frequency). These findings support the validity of the fact that the

underlying physics captured by our results is accurate and physically consistent.

Fig. 7 depicts the relationship between the rotational mass and the moment of inertia of NSs and the corresponding eccentricity of the NSs. It is worth noting that the Eqs. (27) and (39) that help us to calculate the moment of inertia of NSs are only valid for spherical shape. So, to keep the validity of the spherical-body approximation, we set the angular velocity to  $\Omega = 50 \text{ s}^{-1}$ . As shown in Fig. 7(b), the resulting eccentricity values are found to be very close to zero, confirming that the stars remain nearly spherical under this condition. This justifies the continued use of the standard moment of inertia formula. Similar treatments for very slowly rotating NSs have also been employed in Refs. [26, 28], thereby providing precedent and support for our approach.

Our motivation for retaining the investigation of the moment of inertia in this work is to obtain a qualitative insight into the effect of chaotic magnetic fields on the moment of inertia of NSs. Despite the simplification, this still provides a meaningful comparison with moment of inertia constraint, such as that reported in Ref. [27].

Moreover, the study of the moment of inertia, even under the very slow rotation approximation, remains essential in neutron star physics, as it connects to various observable phenomena, such as pulsar glitches (e.g. see Ref. [?]). Since magnetic fields can significantly modify the internal structure and moment of inertia, it is important to assess their qualitative impact, even if only within the slowly rotating approximation.

We can see that at lower masses, the curves of moment of inertia tend to coincide, suggesting that the impact of chaotic magnetic field strength on the moment of inertia is negligible in this regime. However, a noticeable separation begins at  $M = 0.3 M_\odot$ , where the appearance of chaotic magnetic fields lead to a reduc-

tion in the moment of inertia. Given that the moment of inertia depends on both the mass and the square of the radius, these results are consistent with the mass-radius relations.

Remarkably, our findings for the moment of inertia are consistent with the constraint range provided by Landry et al. [27]. It is worth noting that this constraint evaluates whether rotating NSs with chaotic magnetic fields align with observational evidence. The constraint is given as  $I = 1.51_{-0.30}^{+0.20} \times 10^{45} \text{ g cm}^2$  at  $M = 1.4 M_{\odot}$ , the standard canonical mass of NSs. As detailed in Ref. [27], this constraint is derived from measurements of pulsar masses, gravitational wave signals from events such as GW170817 and GW190425, and X-ray data from hotspot emissions on NS surfaces observed by NICER.

## 4 Conclusion

In this study, we calculated the mass and radius of NSs under the influence of a chaotic magnetic field, enabling us to obtain the mass-radius relationship for these stars. Our findings indicate that the magnetic field can decrease the radius of NSs. NSs formed with chaotic magnetic fields exhibit a lower maximum mass compared to those without chaotic magnetic fields. Additionally, while the chaotic magnetic field can contribute to a reduction in radius, it can simultaneously enhance the compactness and deformation of rotating NSs. For deformed rotating NSs, significant deformations occur at lower mass values.

On the other side, our results indicate that the presence of chaotic magnetic field enhances the Kepler frequency of rotating NSs, whereas it simultaneously tend to decrease their moment of inertia. Additionally, the moment of inertia of rotating NSs in our study is consistent with the constraint range obtained from pulsar mass measurements, gravitational wave event data (GW170817 and GW190425), and X-ray observations of emissions from hotspots on NS surfaces measured by NICER.

**Acknowledgements** We sincerely thank Tsuyoshi Miyatsu and Ryan Rizaldy for precious discussions. Special thanks are given to Anna Campoy Ordaz for making her code publicly available, which allowed MLP to modify it for use in this work. MLP acknowledges the Indonesia Endowment Fund for Education Agency (LPDP) for financial support. FPZ and GH would like to thank Kemendiktisaintek (The Ministry of Higher Education, Science, and Technology) of the Republic of Indonesia (through LPPM ITB, Indonesia) for partially financial support. HLP and MLP would like to thank the members of the Theoretical Physics Groups at Institut Teknologi Bandung for their hospitality. MFARS is supported

by the Second Century Fund (C2F), Chulalongkorn University, Thailand.

## References

1. M.L. Pattersons, A. Sulaksono, Eur. Phys. J. C **81** 698 (2021).
2. I. Vidaña, Eur. Phys. J. Plus **133** 445 (2018).
3. A. Reisenegger, ASP Conf. Ser. **248** 469–478 (2001).
4. V. Gruber, N. Andersson, M. Hogg, Int. J. Mod. Phys. D **26** 1730015 (2017). arXiv:1610.06882 [astro-ph.HE].
5. S. Ghosh, S. Shaikh, P.J. Kalita, P. Routaray, B. Kumar, B.K. Agrawal, Nucl. Phys. B **1008** 116697 (2024).
6. C. Sivaram, K. Arun, Open Astron. J. **5** 7–11 (2012).
7. J.M. Cohen, A. Rosenblum, Astrophys. Space Sci. **16** 130–136 (1972).
8. J.E. Horvath, Int. J. Mod. Phys. D **13** 1327–1334 (2004). arXiv:astro-ph/0404324.
9. A. Lyne, F. Graham-Smith, P. Weltevrede, C. Jordan, B. Stappers, C. Bassa, M. Kramer, Science **342** 598–601 (2013).
10. A. Basu, P. Char, R. Nandi, B.C. Joshi, D. Bandyopadhyay, Astrophys. J. **866** 2 (2018).
11. R. Rizaldy, A. Sulaksono, J. Phys. Conf. Ser. **1080** 012031 (2018).
12. B. Franzon, V. Dexheimer, S. Schramm, Phys. Rev. D **94** 044018 (2016).
13. M.L. Pattersons, F.P. Zen, arXiv:2411.11558 [gr-qc].
14. R. Rizaldy, A. Sulaksono, J. Phys. Conf. Ser. **1011** 012083 (2018).
15. G. Desvignes, P. Weltevrede, Y. Gao, et al., Nature Astron. **8** 617–627 (2024).
16. J.F. Fortin, H.K. Guo, K. Sinha, S.P. Harris, D. Kim, C. Sun, Int. J. Mod. Phys. D **30** 2130002 (2021). arXiv:2102.12503 [hep-ph].
17. K. Konno, T. Obata, Y. Kojima, Astron. Astrophys. **356** 234–237 (2000).
18. R. Mallick, S. Schramm, Phys. Rev. C **89** 045805 (2014).
19. J.B. Hartle, Astrophys. J. **150** 1005–1029 (1967).
20. J.B. Hartle, K.S. Thorne, Astrophys. J. **153** 807–834 (1968).
21. L. Lopes, D. Menezes, J. Cosmol. Astropart. Phys. **2015** 002 (2015). arXiv:1411.7209 [astro-ph.HE].
22. D.H. Wen, W. Chen, Y.G. Lu, L.G. Liu, Chin. Phys. Lett. **24** 628 (2007).
23. A.C. Ordaz, Master’s Thesis, Universitat de Barcelona, 2019.
24. L.L. Lopes, Astrophys. J. **966** 184 (2024).
25. F.M. da Silva, L.C.N. Santos, C.C. Barros Jr, Class. Quantum Grav. **38** 165011 (2021).
26. A. Rahmansyah, A. Sulaksono, A.B. Wahidin, A.M. Setiawan, Eur. Phys. J. C **80** 769 (2020).
27. P. Landry, R. Essick, K. Chatzioannou, Phys. Rev. D **101** 123007 (2020).
28. R. Rizaldy, A. Sulaksono, Phys. Rev. C. **109** 025803 (2024).
29. A. Sulaksono, Int. J. Mod. Phys. E **24** 1550007 (2015). arXiv:1412.7247 [nucl-th].
30. B.K. Agrawal, A. Sulaksono, P.-G. Reinhard, Nucl. Phys. A **882** 1–20 (2012).
31. M.L. Pattersons, F.P. Zen, H.L. Prihadi, M.F.A.R. Sakti, arXiv:2404.01837 [gr-qc].
32. M. Dutra, O. Lourenço, S. S. Avancini, B. V. Carlson, A. Delfino, D. P. Menezes, C. Providência, S. Typel, J. R. Stone, Phys. Rev. C **90** 055203 (2014)

---

33. T. Mart, A. Sulaksono, Phys. Rev. C **025807** 025807 (2013). arXiv:1302.6012 [nucl-th].

34. Suparti, A. Sulaksono, T. Mart, Phys. Rev. C **95** 045806 (2017).

35. S. Kumar, R. Bhattacharyya, B. Dasgupta, M.S. Janaki, Phys. Plasmas **24** 082902 (2017).

36. B. Dasgupta, A.K. Ram, G. Li, X. Li, AIP Conf. Proc. **1582** 213 (2014).

37. P. Beltracchi, C. Posada, Phys. Rev. D **110** 024052 (2024).

38. L.M. Becerra, E.A. Becerra-Vergara, F.D. Lora-Clavijo, Phys. Rev. D **110** 103004 (2024).

39. Y.B. Zel'dovich, I.D. Novikov, *Stars and Relativity* (Dover Publications, New York, 1971).

40. J.R. Oppenheimer, G.M. Volkoff, Phys. Rev. **55** 374 (1939).

41. N.K. Glendenning, *Compact Stars: Nuclear Physics, Particle Physics, and General Relativity, Second Edition* (Springer, Heidelberg, 2000).

42. D.H. Wen, W. Chen, L.G. Liu, Chin. Phys. Lett. **22** 1604 (2005).

43. E. Berti, F. White, A. Maniopoulou, M. Bruni, Mon. Not. R. Astron. Soc. **358** 923–938 (2005).

44. L. Kaper, A. van der Meer, M. van Kerkwijk, E. van den Heuvel, The Messenger **126** 27–31 (2006).

45. F. Wu, C. Wu, Z.-Z. Ren, Chin. Phys. C **41** 4 (2017). arXiv:1612.04553 [astro-ph.HE].

46. L.L. Lopes, D.P. Menezes, Eur. Phys. J. A **56** 122 (2020).

47. I.A. Rather, A.A. Usmani, S.K. Patra, Nucl. Phys. A **1010** 122189 (2021).

48. M.C. Miller, F.K. Lamb, A.J. Dittmann, S. Bogdanov, Z. Arzoumanian, K.C. Gendreau, S. Guillot, W.C.G. Ho, J.M. Lattimer, M. Loewenstein, S.M. Morsink, P.S. Ray, M.T. Wolff, C.L. Baker, T. Cazeau, S. Manthripragada, C.B. Markwardt, T. Okajima, S. Pollard, I. Cognard, H.T. Cromartie, E. Fonseca, L. Guillemot, M. Kerr, A. Parthasarathy, T.T. Pennucci, S. Ransom, I. Stairs, Astrophys. J. Lett. **918** L28 (2021).

49. T.E. Riley, A.L. Watts, A.V. Bilous, P.S. Ray, S. Bogdanov, Z. Arzoumanian, D. Choudhury, S. Guillot, J.S. Deneva, S.M. Morsink, K.C. Gendreau, A.K. Harding, W.C.G. Ho, J.M. Lattimer, M. Loewenstein, R.M. Ludlam, C.B. Markwardt, T. Okajima, C. Prescod-Weinstein, R.A. Remillard, M.T. Wolff, E. Fonseca, A. Parthasarathy, H.T. Cromartie, S. Ransom, I. Stairs, M. Kerr, T.T. Pennucci, L. Guillemot, I. Cognard, Astrophys. J. Lett. **918** L27 (2021).